The influence of large second phase grains on microstructural evolution during diffusion creep

***Joe Gardner*[a*]*, John Wheeler*[a]

[a]Department of Earth, Ocean, and Ecological Sciences, University of Liverpool, 4 Brownlow Street, Liverpool, L69 3GP, UK

*corresponding author email: jgardner@liv.ac.uk; Tel: +447969156667

Other author emails: johnwh@liv.ac.uk

Keywords: diffusion creep, pressure solution, crystallographic preferred orientation, microstructural evolution, numerical modelling

Abstract

Diffusion creep is a fundamental mechanism by which Earth materials deform, but the way microstructure evolves during diffusion creep remains poorly understood, because the mechanism does not leave behind abundant microstructural indicators. Because most rocks are polyphase, this study used numerical simulations to investigate the influence of large second-phase grains on the microstructural evolution of a fine-grained matrix during diffusion creep in both pure and simple shear. The results of the modelling show that large second-phase grains create stress heterogeneities that focus the effects of diffusion creep, which can lead to a profound drop in strength of a material, and dictate where grain boundary sliding surfaces develop within the fine-grained matrix. Rotations of matrix grains are strongly influenced by the rotation direction and velocity of the large grain, especially those that lie adjacent to it. The rotation direction of large grains is not simply either synthetic or antithetic to the shear direction. Instead, rotation directions of large grains can change due to interactions with the matrix. Such interactions could result in simple strain paths producing complex microstructures which could be misinterpreted to record much more complicated strain histories.

1 Introduction

The geodynamic behaviour of the Earth is dependent on the physico-chemical properties of the Earth material being deformed, which itself is dependent on that material's metamorphic and deformation history. A rock's microstructure (texture) contains detailed information about the deformation and metamorphic processes that were operative during its history, provided geologists can correctly interpret the microstructural features. One aspect of textural interpretation that remains elusive is exactly how a microstructure evolves during diffusion creep.

Diffusion creep is a fundamental process in the Earth's lower mantle (Ammann et al., 2010; Karato and Li, 1992; Karato et al., 1995; Mohiuddin et al., 2020; Ritterbex et al., 2020), upper mantle (Hiraga et al., 2010; Hirth and Kohlstedt, 1995; Karato and Wu, 1993) and crust (Bell and Cuff, 1989; Kilian et al., 2011; Rosenberg and Stünitz, 2003; Rybacki and Dresen, 2000; Rybacki et al., 2006). In the mid-to-upper crust (to a depth of some 20 km), water is abundant. For example, in the fractured upper crust, an interconnected, fluid-filled network of pores characteristically makes up on the order of 1 vol%, and the crust behaves hydrologically like a homogeneous infinite aquifer (Bucher and Stober, 2010). Porosity vanishes below the brittle-viscous transition (~12–15 km depth) but water remains adsorbed to grain boundaries, and occurs in hydrous phases and fluid inclusions (Bucher and Stober, 2010). In the presence of fluid, diffusion-dominated deformation is termed pressure solution or dissolution-precipitation creep (Menegon et al., 2008; Rutter, 1976; Rutter, 1983; Wheeler, 1992; Wintsch and Yi, 2002). It is important to recognise that pressure solution occurs by diffusion of material along stressed H_2O-rich grain boundary films, which have different physical properties and chemical behaviour to pockets of fluid that, for example, may collect in pores (Gratier et al., 2013; Wheeler, 1992). Hence, the processes of pressure solution and diffusion creep are equivalent and can be described by exactly the same equations (Elliott, 1973). The presence or absence of

a crystallographic preferred orientation (CPO) is commonly used to distinguish deformation by dislocation creep and diffusion creep. During dislocation creep a CPO is developed due to slip on specific crystallographic planes and in specific crystallographic weakening directions (Karato et al., 2008). During diffusion creep, a CPO is traditionally not expected to develop, and any pre-existing CPO is expected to be diminished or destroyed by rotations associated with grain boundary sliding (GBS), which is required for the material to maintain continuity during grain shape change (Elliott, 1973). The dominant deformation mechanism by which different parts of the mantle deform is inferred from an observed presence or absence of seismic anisotropy, where its presence is interpreted to be a product of preferentially aligned crystals, indicating dislocation creep (e.g. Karato et al., 2008; Skemer and Hansen, 2016). Where seismic anisotropy is absent, diffusion creep has been proposed to dominate deformation (Karato and Wu, 1993).

Recent advances in our understanding of how diffusion creep operates in rocks have brought some of these ideas into question. A growing list of authors have reported evidence of CPOs developing during diffusion creep under specific conditions (Bons and den Brok, 2000; Díaz Aspiroz et al., 2007; Getsinger and Hirth, 2014; Gómez Barreiro et al., 2007; Imon et al., 2004; Miyazaki et al., 2013; Shelley, 1977; Sundberg and Cooper, 2008). More pertinent to the current study are results that show a CPO can be preserved or modified without being wiped out during diffusion creep. For example, Jiang et al. (2000) showed that an inherited CPO could be preserved to high strain in albite during diffusion creep. Wheeler (2009) used a numerical model to show that seismic anisotropy could be preserved during diffusion creep in a monophase material due to the suppression of grain rotations during deformation. Grain rotations were inhibited by slight elongation of grains, which occurred when diffusion creep rates were fast compared to grain growth rates. Grain elongation occurs during diffusion creep because dissolution at faces experiencing highest normal stress and precipitation at faces

78 experiencing lowest normal stress results in ‘flattening’ of grains (e.g., Rutter, 1983). Grain
79 growth, or annealing, results in more equiaxed grains, so if this is fast compared to diffusion
80 creep, grain elongation is inhibited (Wheeler, 2009). In contrast to such observations, Elliott
81 (1973) noted that if the strain path during diffusion creep is coaxial and grains do not rotate,
82 then as grains become more elongate, diffusion paths will get longer, and so the process in
83 theory could become self-exhausting. In practice this does not happen, because even on a
84 coaxial strain path, grains continuously rotate with respect to each other because of GBS. Such
85 rotations bring different crystal faces into contact, so newly precipitated parts of grains become
86 subject to dissolution, which tends to keep grains equiaxed. For the most part, coaxial
87 deformation is a rare case, only occurring locally within a body of deforming rock, and bulk
88 coaxial deformation in natural rocks is often partitioned into zones of opposite-sense non-
89 coaxial strain (e.g. Bell et al., 2004). Typical non-coaxial strain paths will tend to keep grains
90 equiaxed. Thus, the link between diffusion creep, grain rotations, and CPO development,
91 preservation and/or annihilation remains ambiguous.

92 Nearly all rocks are polyphase, and a number of previous numerical models have explored the
93 interaction between different phases during deformation (e.g. Carreras et al., 2013; Dabrowski
94 et al., 2012; Jessell et al., 2009 and references therein; Johnson, 2008). The rotation behaviour
95 of large rigid grains embedded in a lower viscosity fine-grained matrix during deformation has
96 been of particular interest because large grain rotations can record regional-scale strain
97 histories (e.g. Holcombe and Little, 2001; Passchier and Trouw, 2005, and references therein).
98 Microstructures such as spiral garnets have commonly been interpreted to record substantial
99 rotation of porphyroclasts (Rosenfeld, 1970), although debate remains as to whether such
100 patterns truly record rotation of large grains relative to geographic coordinates (e.g., Aerden
101 and Ruiz-Fuentes, 2020; Bell and Johnson, 1989; Johnson, 1993; Williams and Jiang, 1999).
102 However, previous studies of inclusion trails have also shown that rotation of large grains can

be supressed in deformed metamorphic rocks. For example, Steinhardt (1989) showed that porphyroclasts in non-coaxially deformed schists had undergone very little or no rotation during deformation relative to one another on the scale of an entire outcrop (tens of metres). Studies on the regional scale have also shown a lack of porphyroblast rotation in the Otago schists (Johnson, 1990; inclusion trails consistently oriented over 3000 km^2), the Lys-Caillaouas Massif in the Variscan Pyrenees (Aerden, 1995; inclusion trails consistently oriented over tens of km^2), the Variscan Iberian Massif (Aerden et al., 2020), and many other places (see references in Fay et al., 2008 for other examples).

As a result of the controversy surrounding whether rigid objects rotate or not during non-coaxial deformation, a large number of modelling studies have focused on the issue. A summary of the previous literature can be found in Table 1 of Griera et al. (2013). For example, Fay et al. (2008) used finite element modelling of material with Mohr-Coulomb plasticity to show that anastomosing shear zones can develop around large strong rigid objects in a relatively fine-grained and weak matrix, because of stress concentrations generated around the large grains during initial shortening. When shear zones develop, no large grain rotation occurred, and if such shear zones were absent, large grains did rotate. Griera et al. (2011) note that experiments and numerical simulations that use viscous matrix rheologies result in the rotation of porphyroclasts, whereas those using Mohr-Coulomb rheologies generally result in non-rotation. Using a full-field crystal plasticity method in the *Elle* microstructural modelling suite (Bons et al., 2008), Griera et al. (2011) explored the effects of an anisotropic polycrystalline matrix deforming by dislocation creep on large grain rotation. Their results suggested that the rotation of large grains is strongly dependent on the degree of anisotropy in the matrix grains, with more anisotropic matrix grains leading to the development of shear bands that inhibit the rotation of large grains.

Numerical models of large grain rotations in a matrix deforming by diffusive mass transfer are so far lacking. In diffusion creep, Wheeler (2009) showed that grain elongations do not have to be very large before they significantly impact grain rotations in monophase aggregates, but microstructural evolution within a polyphase sample depends strongly on how the different phases interact mechanically (e.g. Jessell et al., 2009). The viscosity of a polymineralic rock undergoing pressure solution can be much lower than its monomineralic counterparts, as predicted theoretically (Wheeler, 1992) and observed in experiments (Sundberg and Cooper, 2008; Zhao et al., 2019). Grain boundary diffusion creep is also more efficient in fine-grained rocks as the length of diffusion pathways (i.e. grain boundary segments) are small, so the inhibition of grain growth by boundary pinning affects creep rates in multiphase materials. Variation in grain size within a sample may have a local effect on distribution of stress, and therefore how a given microstructure responds to an imposed far-field stress. Many of the factors that control how the microstructure of a polyphase rock may evolve during diffusion creep remain to be tested.

Previous attempts at modelling the influence of a large second-phase grain on the evolution of a polycrystalline material deforming by diffusion creep have been made using the same modelling software employed in this study (described fully in section 3). Berton et al. (2006) investigated the development of fibrous pressure shadows at the interface between a rigid object and a fine-grained matrix of different compositions in a two-phase composite deforming by pure shear. Those authors showed that the ratio of $CaCO_3$ diffusion rate along calcite-pyrite versus calcite-calcite boundaries strongly influenced pressure shadow growth, sliding and rotation of matrix grains, and the orientation of strain axes around the rigid object, which suggests that purely physical models of ductile flow around rigid clasts in rocks do not capture the complexity of microstructural evolution during diffusive mass transfer-driven deformation.

Berton et al. (2011) advanced these conclusions by exploring the effects of inclusion size and boundary smoothness on pressure shadow growth, again during pure shear.

Here we present the first models for the effects of a large grain sitting in a fine-grained matrix of different mineralogy, during deformation by diffusive mass transfer in both pure and simple shear. We show how rotations and angular velocities of both the matrix grains and the large grain evolve with increasing strain, and discuss how such changes affect CPO modification and stress evolution in the model.

2 Fundamental aspects of pressure solution and grain boundary diffusion (Coble) creep

Elliott (1973) showed that the processes of pressure solution and grain boundary diffusion creep are equivalent, and flow laws have the same mathematical form, except that pressure solution may be faster due to fast diffusion along aqueous grain boundary films rather than along essentially dry grain boundaries. The most fundamental link between stress (a physical property) and diffusion (a chemical process) comes from the driving force for diffusion, which is the gradient in chemical potential, μ, defined as:

$$\mu = F + \sigma_n V \quad (1)$$

where σ_n is compressive normal stress across the interface, F is the molar Helmholtz free energy of the solid, V is the molar volume of the solid. Strictly, μ is the chemical potential of the solid in an adjacent 'phase' in which it can dissolve, and the 'phase' in this case is actually the grain boundary region. Eq. (1) shows that as normal stress increases on an interface, the chemical potential of the material next to that interface will also increase, that is it will dissolve more readily. Grain boundaries under higher normal stress will therefore have a higher chemical potential than grain boundaries under lower normal stress, which in turn results in a gradient in chemical potential along grain boundaries, and between different boundaries of the same grain (Fig. 1a). These gradients drive diffusion of material resulting in shape change. Variations

175 in normal stress can then give rise to gradients along interfaces (enabling Coble creep) and
176 within grains (enabling Nabarro-Herring creep).

177 Building on this fundamental relationship between stress and diffusion, Coble (1963) analysed
178 diffusion creep of spherical grains of diameter *a* to find a linear relationship between stress and
179 strain rate for pure shear. This relationship was revised by Raj and Ashby (1971) and Poirier
180 (1985), and can be rewritten in terms of the shear stress to obtain the equivalent Newtonian
181 viscosity η (following Eq. (7.14) of Poirier, 1985):

182 $$\eta = \frac{1}{141}\frac{kTa^3}{Dw\Omega} = \frac{1}{141}\frac{RTa^3}{Dw\mathrm{V}} \qquad (2)$$

183 where *k* is Boltzmann's constant, R is the gas constant, *T* is temperature, *w* is grain boundary
184 width, *D* is the diffusion coefficient, Ω is atomic volume, *V* is molar volume and *a* is grain size
185 (diameter). This derivation assumed a spherical grain embedded in a medium with a simple
186 stress system, so does not encompass the actual geometries of interlocking grains. To address
187 this, Raj and Ashby (1971) modelled arrays of regular hexagons, but in such models each grain
188 is identical and behaves the same way, so processes such as the reduction of CPO strength by
189 grain rotation cannot be modelled. In such models, either the grains do not rotate and instead
190 become elongate if grain boundary sliding is allowed to occur by two orthogonal 'modes' of
191 sliding, or all the grains rotate the same amount and need not show any shape change, if sliding
192 occurs by one dominant mode (Raj and Ashby, (1971). Ford et al. (2002) and Ford et al. (2004)
193 thus went further, to model an arbitrarily complex space-filling array of grains. The model was
194 extended to include an insoluble second phase (Berton et al., 2006; Berton et al., 2011), and to
195 encompass spatially periodic microstructures (Wheeler 2009).

196 Grain boundary sliding is intrinsic to diffusion creep (Raj and Ashby, 1971). This leads to
197 collisions between triple junctions followed by neighbour switching, as first modelled by

198 Ashby and Verrall (1973). Spingarn and Nix (1978) pointed out the grain shape change during
199 neighbour switching predicted in Fig. 4 of Ashby and Verrall (1973; redrawn in Fig. 1b) was
200 incorrect, and presented a correct model, as shown and described in Figure 1c. Our modelling
201 reproduces that behaviour when starting with a microstructure of regular hexagons. Some
202 previous modelling of diffusion creep has encompassed finite grain boundary sliding viscosity
203 (Wheeler 2010). This leads to a modified grain size dependence in the flow law, for which
204 there is no clear support from experiments, and in the current model we set the grain boundary
205 shear stress to zero.

206

207

208

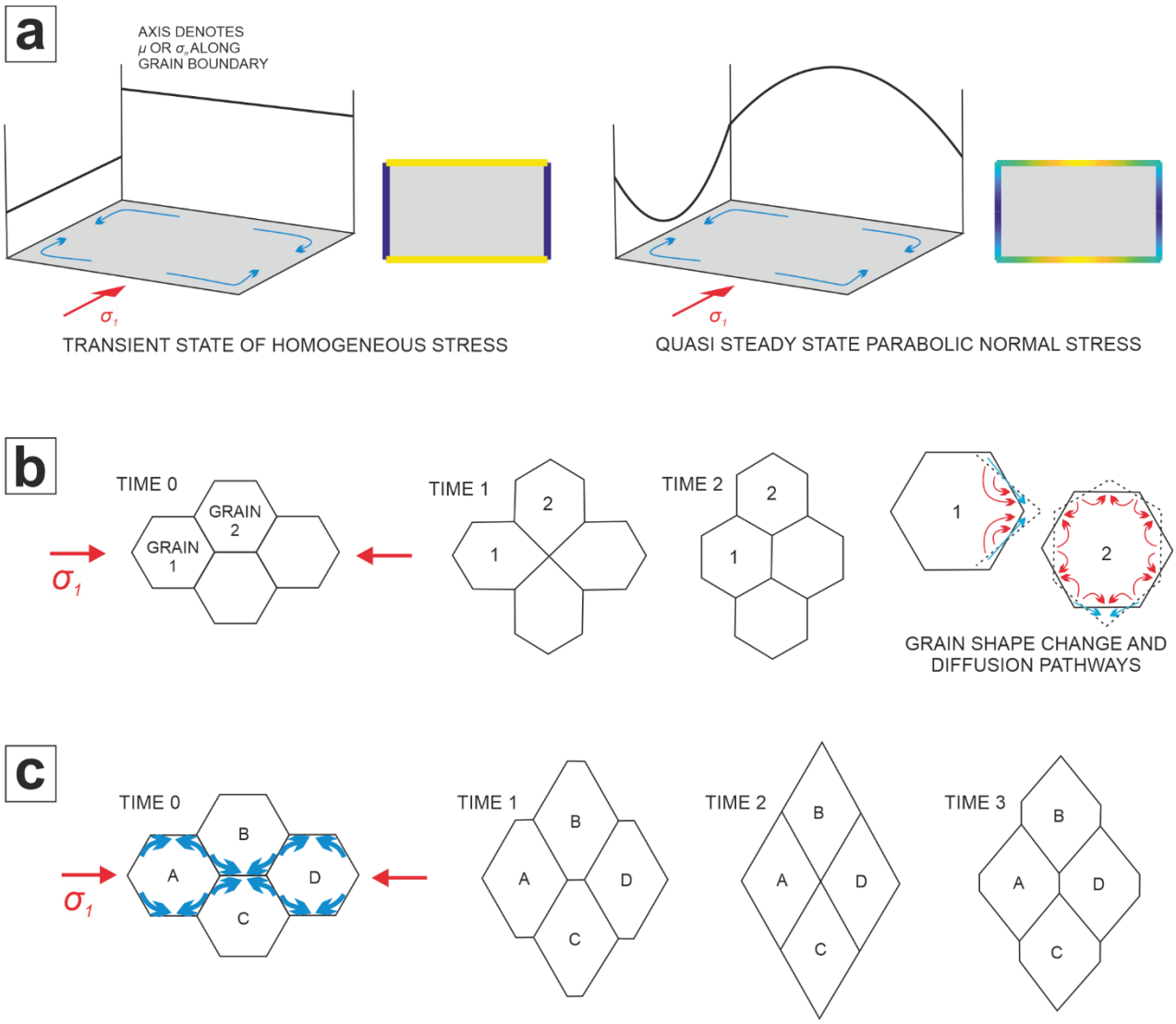

Figure 1 *Stresses and neighbour switching during diffusion creep. a) Initial and steady state stresses during diffusion creep of a rectangular grain microstructure. Normal stress evolves to a parabolic distribution during diffusion creep or pressure solution, and is visualised either by plotting it in the third dimension (redrawn from Fig. 1 of Wheeler, 1992, and see "Stresses" movies in the supplementary information), or colour coding it along boundaries in 2D (as used in Figs. 5 and 9). b) Shape change at three consecutive stages during diffusion creep, as represented incorrectly in the Ashby-Verrall neighbour switching model (redrawn from Figs. 4 and 7 of Ashby and Verrall, 1973). Dashed boundaries show final grain shape, red curved arrows show bulk diffusive flux, blue straight arrows show boundary diffusive flux. The model cannot be right because grains begin with identical shapes and are subject to*

identical imposed stress, yet grain shapes are then illustrated as evolving differently (for details see Spingarn and Nix (1978)). c) Progressive shape change during neighbour switching in diffusion creep is correctly depicted in Fig. 7 of Spingarn and Nix (1978); slightly modified here to highlight boundary diffusive flux pathways (blue arrows). All fluxes are symmetric and grains evolve in identical ways in accord with their identical initial shapes. For initial regular hexagons the DiffForm modelling software reproduces the evolution shown. Spingarn and Nix add a final stage in which interface energy plays a role, but this is not included in our current model.

Wheeler (1992) found it useful to use Onsager diffusion coefficients *L (= Dc/RT)*, where *D* is the conventional diffusion coefficient, *c* is concentration, *R* is the gas constant, and *T* is absolute temperature, to describe diffusion of each chemical component during creep in multiphase systems. *D* as used in Fick's law is insufficient to model diffusion creep as it represents diffusion proportional to a gradient in concentration, whereas diffusion in solid-state systems is more accurately described by assessing gradients in chemical potential, μ. μ is incorporated into the Onsager diffusion coefficient so its use is more appropriate than *D* in models of solid-state diffusion. When multiplied by grain boundary width *w*, $A = wL$ describes the overall ease of diffusion along a boundary (Eq. (4) in Wheeler, 1992). The net chemical current along a grain boundary is a function of the 'conductances', *A,* of all components that comprise the system. With several chemical components, *A* is a matrix and it proves useful to define its matrix inverse, *K* (Eq. (5) in Wheeler, 1992). *K* values relate to the 'resistances' (or the inverse of the 'conductances') of each component to dissolution or growth by diffusion along the grain boundary (Wheeler, 1992). In the model we discuss here, the second phase is insoluble and the mathematics is simplified. With one soluble phase we define one chemical component with a

formula identical to that phase, and $K = 1/A$ (Eq. (6) of Wheeler, 1992). This means that for spherical grains, from Eq. 2:

$$\eta = \frac{1}{141}\frac{RTa^3}{Dw\Omega} = \frac{1}{141}\frac{a^3}{wL\dot{V}^2} = \frac{1}{141}\frac{Ka^3}{\dot{V}^2} \quad (3)$$

The model we present is grain scale and so provides precise details of grain rotations and viscosity evolution. The viscosity still scales with grain size etc. in accord with Eq. 3 but the key enhancement is that the single dimensionless number here (1/141) is replaced by an evolving and anisotropic function of microstructure. Elliott (1973) recognised that evolving grain shape changes viscosity; our model captures the more general dependence on microstructure. In addition, Wheeler (2010) showed that mechanical anisotropy develops during diffusional creep that includes a component of boundary sliding, which it always does (Raj and Ashby, 1971). The consequence of this is that as grain rotations occur, grains can become aligned in 'weak' or 'strong' directions with respect to the direction of maximum shortening. Consequently, the viscosity at each time depends on the microstructure and the orientation of strain rate axes relative to that microstructure. Eq. 3 provides a "benchmark" value for comparison between idealised spherical grains and more complex microstructures with the same average grain size.

3 Methods

Diffusion creep modelling was performed using the C++-based modelling suite DiffForm, and the results were visualised in MATLAB® using the DiffView software (Berton et al., 2006; Berton et al., 2011; Ford et al., 2002; Ford et al., 2004; Wheeler, 2009; Wheeler and Ford, 2008). A rigorous treatment of the fundamental mathematics used by DiffForm can be found in Wheeler and Ford (2008) and Wheeler (2009)**.** The intention here is to attempt to describe how DiffForm works in a way accessible to non-mathematicians, to emphasise the physical processes that are being modelled.

Wheeler (1987) showed that the ideal distribution of stress (i.e. the chemical potential) along a boundary has a parabolic shape (Fig. 1a; distribution is cubic if there are relative grain rotations), toward which all other stress distributions evolve, with the consequence that material can be dissolved or precipitated at all points along the boundary. The flux, and therefore the current (i.e. the flux × the boundary width; Wheeler and Ford, 2008), can be determined at any point along the boundary, so dissolution and precipitation rates can be calculated for a given imposed normal stress. The divergence speed of any two adjacent grains can be calculated from the dissolution and precipitation rates at grain boundaries. Because grains are rigid and do not experience internal deformation, the relative motions of grains must be equivalent to their relative velocity plus a rotation around a reference point. As no internal deformation is assumed by the model, overgrowths must be either of constant width or wedge-shaped.

A set of simultaneous equations are solved to determine instantaneous velocities and angular velocities of grains, and stresses along each boundary. After each strain increment is applied, the microstructure is modified by repositioning grain boundaries in the middle of overgrowths and regions of dissolution. Triple junctions that overlap at any stage, representing the neighbour switching events common to GBS (Spingarn and Nix, 1978) are redrawn. The resultant microstructure is then used to solve for new velocities and streshses. Note that stress is not actually imposed on the model microstructure; instead an average strain rate tensor is imposed, for which the simultaneous equations are then solved to predict the average stress and the local stresses on grain boundaries, which in turn drive shape change.

There are three inputs to the program.

Input 1. The initial grain geometry ("net") shown in Figure 2 was used to test how the presence of a large second phase grain might impact the microstructural evolution of a fine-

grained monophase matrix deforming by diffusion creep. This starting "net" was translated into the input format used for DiffForm from the input format used for Elle (Piazolo et al., 2010). This topology is roughly analogous to the porphyroclasts/blasts often found in metamorphic rocks, or the phenocrysts commonly observed in igneous lithologies. The matrix grains are designed to exhibit a shape preferred orientation, or shape fabric, which is again commonly observed in both metamorphic and igneous rocks. The shape fabric of the matrix is simplified to allow clear identification of any effects the large grain may have on matrix-grain evolution. The possible effects of the matrix grains all having exactly the same shape, size and shape orientation, compared to the heterogeneity of grain shape and size found in natural samples, is discussed in section 5.4.

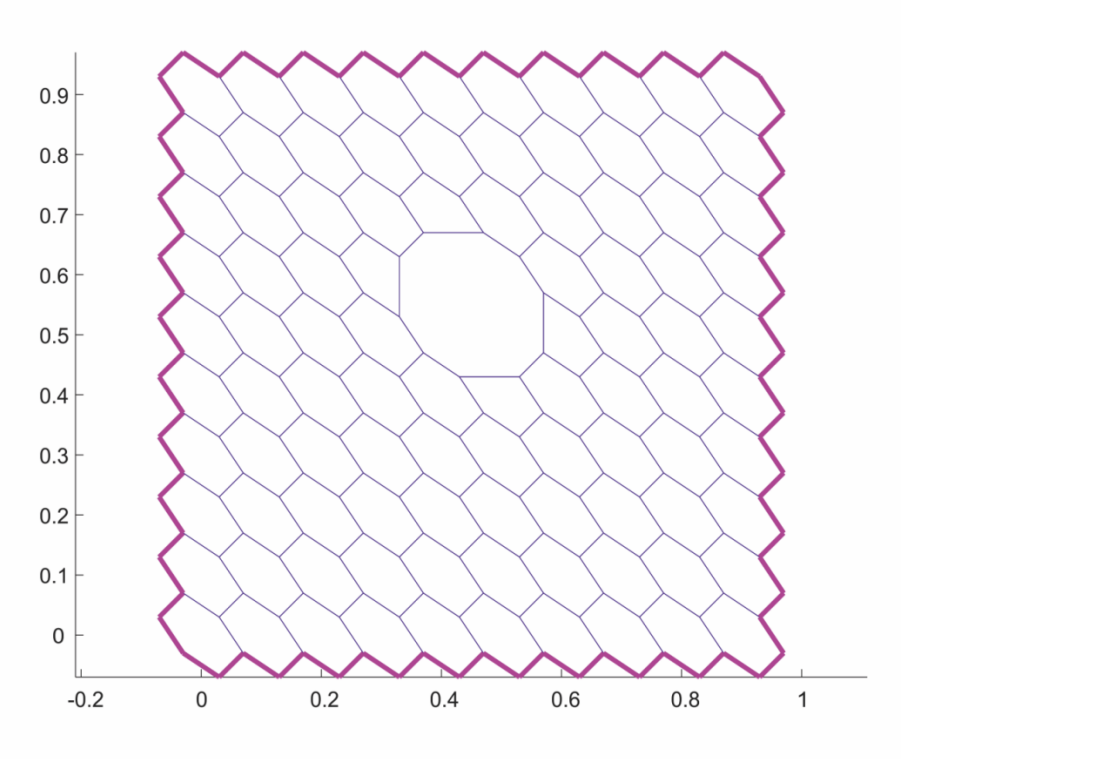

Figure 2 *Starting geometry of model runs. Blue lines represent grain boundaries. The large central grain is defined to be of a different composition to the matrix grains. Scale is arbitrary in the model.*

Input 2. 'K values' (resistances) for each component and molar volumes for each phase. Here the second phase is required to be insoluble, but this would imply an infinite *K* so instead the *K* value is set to a large but finite value. A key point is that model outputs scale in a simple way with regard to parameters. The stress scales in accordance with Eq. 3. Grain angular velocities scale in accordance with strain rates, for each particular imposed strain geometry. This means that the choices for *K*, *V* and the grain size in the starting net will not affect the model outputs, except for the stress levels, for which scaling is simple.

With this in mind 'legacy' values of various coefficients are used in the program. In the model runs presented here, the matrix grains were defined to have the composition of calcite, $CaCO_3$, and the large grain was defined as pyrite, FeS_2. These were used in Berton et al. (2006) and have not been changed subsequently, but we emphasise that our models make predictions about any insoluble mineral embedded in any mineral that is undergoing pressure solution or diffusion creep. The parameters used in the DiffForm input file for our experiments are:

Average grain area for soluble phase $G = 0.01$ m^2

Diameter of equivalent circle $a = ((4/\pi)G)^{1/2} = 0.112$ m

$V = 3.693 \times 10^{10}$ m^3/mol

$K[CaCO_3, CaCO_3] = 2 \times 10^{18}$ Pa.s m^3 mol^{-2}

From which we find, from Eq. 3, a viscosity for equivalent spherical grains of 1.461×10^{-8} Pas – unrealistically small but needed only as a benchmark with which to compare model outputs.

Input 3. Strain geometry, rate and timestep. In all experimental runs presented here, the starting net was set up to undergo at least 200 increments of either pure or simple shear at a strain of 0.5 per time step, with a time step length of 0.01 s. Multiplying strain by time step length results in a strain of 0.5% being imposed on the model per time step, so that 100% strain

would be achieved after 200 time steps). Time step length, and therefore strain rate, are arbitrary as there is a linear relationship between angular velocity and overall strain rate in the model (note this is on the scale of the whole model, as opposed to the angular velocities of individual boundaries. In our model, boundaries cannot be used as passive markers as grains undergo dynamic shape change), so faster strain rates simply mean the microstructural evolution occurs more quickly, but the final microstructure produced is identical (see Wheeler, 2009, for more details).

One consequence of the legacy coefficients is that values for stress in the model are small. The stress evolution of the model runs presented here are discussed fully in section 5.3. The small values for stress do not affect the predictions of how the microstructure evolves, since these depend on finite strain and are independent of strain rate; nor do they affect the predicted angular velocities, since these scale with strain rate.

DiffForm models are spatially periodic (in essence, infinite) thus avoiding the undue influence of model boundaries in small finite models. The model tracks changes in the starting microstructure as it evolves along either coaxial (pure shear), non-coaxial (simple shear), or mixed strain pathways. DiffForm has been continually developed over the last two decades (Berton et al., 2006; Berton et al., 2011; Ford et al., 2002; Ford et al., 2004; Wheeler, 2009; Wheeler and Ford, 2008), with the most recent advancements allowing the modelling of two-phase materials. Due to computational limitations, some starting geometries terminate after accumulating only very small strains. Once a starting geometry that can accumulate high strains has been defined, the time required for each model run is on the order of a few days.

In the model runs presented here, the matrix grains have a shape-preferred orientation. This helps to give each grain an anisotropic rheology, which is common in natural crystals, and a key component of accurately modelling the deformation of polycrystals (e.g. Griera et al.,

2013). Although the strong SPO is a simplification of the greater shape heterogeneity observed in natural microstructures, the effects of which are discussed in section 5.4.1, to our knowledge this is the first study that presents results of the effects of a matrix with anisotropic rheology deforming by diffusion creep on the rotation behaviour of a large rigid object.

4 Results

4.1 Pure shear

The starting net shown in Figure 2 was deformed in both pure and simple shear. The model output files presented in the figures, together with software ("DiffView") allowing visualisation of grain movements, stresses, and so on are available from the authors on demand. Numerical experiments performed using DiffForm eventually terminate because of problems with the evolving topology of the net (neighbour switching in particular; see section 5.4). If these occur at the edge of the net as represented in the model, there are a number of scenarios and some are difficult to deal with, hence the program terminates. The pure shear experiment terminated at 130 time steps, i.e. achieved a strain of 65%. Four strain increments of the microstructural evolution are presented in Figure 3a–d. Grains in Figure 3 are coloured by the finite rotation they have undergone from their original orientation, in degrees (readers are referred to the Pure_fin_theta simulation in the supplementary materials for an animation of evolution of finite rotations throughout the entire experiment). Note that the colour scale changes for each strain increment presented in Figure 3, to allow visualisation of larger finite rotations as deformation proceeds. The colour scale limits are set to the maximum rotation in each frame, and are changed in each plot so that the contrast between the largest and smallest rotations at each time increment can easily be seen. In contrast, the animations in the supplementary materials are set up so that the colour scale limits are the same for all frames. This leads to differences in rotations in the earliest stages of the model run being somewhat obscured by the colour scheme, because the rotations are small relative to the colour scale

limits. Figure 3a shows that, by a strain of about 0.16, most matrix grains have rotated about the same amount as the large grain (~15°), with the exception of a row of grains whose rotations appear to be subdued by their alignment with the long axis of the large grain (at an angle of approximately 55° to the direction of maximum shortening) and so have only rotated some 10°. Figure 3b shows a similar trend, with distinct regions of the matrix undergoing different finite rotations depending on their geometric relation to the large grain. The band of lowest rotations sits at 60° to the maximum shortening direction. By a strain of about 0.49 (Fig. 3c), the band has flattened to around 70° with respect to the maximum shortening direction, but the influence of the large grain is no longer apparent along the entire band. Instead, most matrix grains that do not neighbour the large grain have rotated more (some 45°) than the large grain itself (closer to 35°), and matrix grains that neighbour the large grain either have lower or higher finite rotations than the bulk matrix. By the last stage, a 'sliding surface' (perhaps a shear band) that links up across multiple grains has formed (this is best seen in the animation in the online supplementary information), at an angle of 75° to the maximum shortening direction (Fig. 3d). The sliding surface is composed of aligned boundaries of grains that undergo the smallest rotations in the early stages of deformation, so its development is fundamentally related to the presence of the large grain. By the time the model terminates, it has undergone a longitudinal strain of roughly 0.65. The model retains a constant area, a useful check that the mass conservation equations built into the code are satisfied. We note that under certain conditions (e.g. cleavage development as described in Bell and Cuff, 1989), pressure solution can result in substantial volume loss; here we are considering the simplest case.

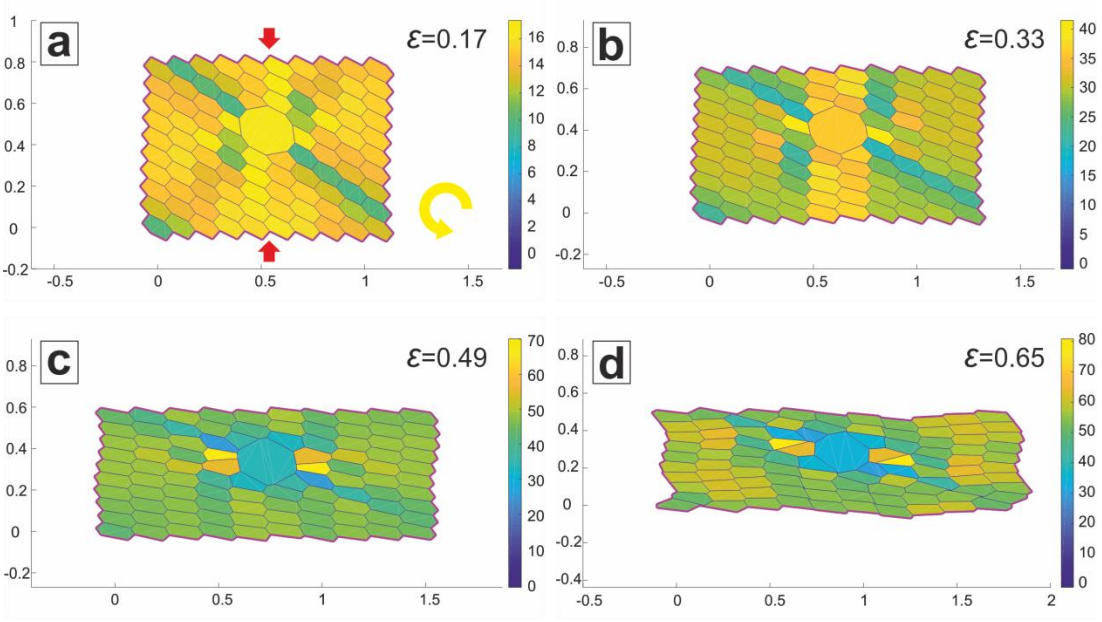

Figure 3 *Results of the pure shear experiment at four strain increments. The model terminated at a strain of 0.65. Grains are coloured by finite rotation with respect to starting orientation in degrees (anticlockwise positive; yellow arrow in (a)). Red arrows in (a) show direction of shortening. Note change in scale for each strain increment; colour scale was altered so unique features can be seen at each stage. For an animation of finite rotations throughout the entire evolution of the model, see the Pure_fin_theta simulation in the supplementary materials.*

Figure 4a shows a plot of the finite rotations of each grain with respect to their initial orientation, with the rotation behaviour of the large grain highlighted as a thick red line. A thick blue line shows the mean rotation behaviour of all matrix grains. Notably, most matrix grain rotations tend to steadily increase in an anticlockwise direction with increasing strain (anticlockwise rotation is defined as positive). This is interpreted to be an effect of the orientation of the strong shape fabric in the matrix with respect to the direction of maximum shortening, and more variation in rotations might be expected in model nets with more heterogeneous grain shapes. The large grain begins rotating in the same, anticlockwise, direction as the matrix grains, but at a strain of about 37% its direction of rotation reverses.

This is reflected in a plot of the angular velocities of all grains (Fig. 4c), where the rotation velocity of the large grain initially accelerates, before stabilising at around 60° per arbitrary time unit at a strain of approximately 0.1. The grain then slows and eventually reverses its rotation direction at a strain of 0.37. At this point the red line in Figure 4c crosses the dashed line representing zero angular velocity, as the grain switches from positive to negative rotation.

The large grain then begins to accelerate in the new rotation direction until it reaches about 25° per time unit (Fig. 4c), before slowing to around 30° per time unit at a strain of around 0.4. Between 0.4 and 0.6 strain, the large grain's angular velocity is somewhat erratic, first slowing by about half and then accelerating sharply at around 0.56 strain. The large grain rapidly reverses rotation direction again just before failure after achieving a strain of 0.6. Overall, the matrix grains experience a less variable rotation history, with the majority of grains rotating at a fairly constant angular velocity of around 50° per time unit (blue line in Fig. 4c), until a strain of around 0.45. After a strain of 0.45 is reached, this steady-state behaviour in the angular velocities of the matrix grains comes to an end and nearly all grain rotations slow down (mean angular velocity drops to around 20° per time unit; blue line in Fig. 4c), before the matrix grain population undergoes a wide spread in accelerations/decelerations at a strain of about 0.6, just before the model terminates. The spread in angular velocities of the matrix grains appears to be caused by the acceleration in angular velocity of the large grain, which begins just before 0.6 strain, and influences matrix grains directly adjacent to it, which then undergo relatively turbulent behaviour compared to grains in the bulk matrix. The large spread in angular velocities of the matrix grains at the end (after 0.6 strain) of the pure shear experiment is qualitatively similar to a large spread in angular velocities of matrix grains at the beginning (~0.1 strain) of the simple shear experiment (see section 4.2). In simple shear, the spread in angular velocities of matrix grains is observed to be associated with a change in angular velocity of the large grain, and a drop in overall strength of the model net. However, because

the model terminates directly after this spread occurs in the pure shear model, it is not possible to observe or predict whether angular velocities of grains would return to steady-state behaviour in pure shear. Likewise, mean matrix grain rotations suggest that the microstructure may be asymptotically approaching a rotational steady-state as per Wheeler (2009), but termination of the model makes this difficult to be sure of. Readers are referred to the Pure_fin_theta simulation in the supplementary materials for an animation of angular velocity evolution throughout the entire experiment.

The development of the sliding surface by grain boundary alignment has a profound effect on the strength of the model. Differential stress steadily increases with increasing deformation until a critical point, just after a strain of 0.5, is reached (Fig. 4d), i.e. just after the steady-state behaviour of the matrix grains observed in the angular velocity plot ends. As the model terminates, the differential stress evolves along a stress-strain path reminiscent of typical rock deformation laboratory experiments stressed to brittle failure (e.g. the room temperature experiments performed by Tullis and Yund, 1992; see their Fig. 3). The stress-strain curve shows the strength of the material, which initially increases, before dropping substantially just after a strain of 0.5, just before the model run terminates.

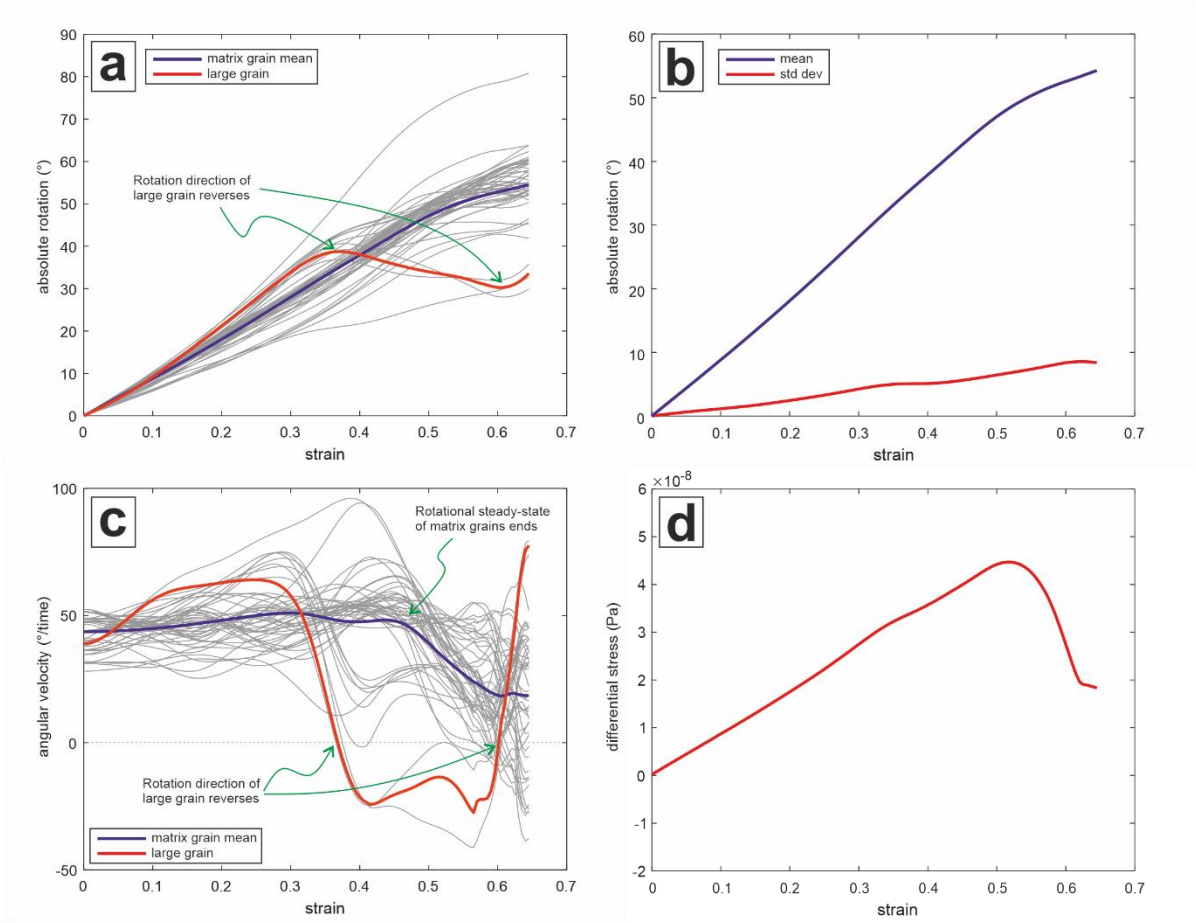

458

459 ***Figure 4*** *a) Absolute rotation in degrees of each grain (grey lines) as a function of increasing*
460 *strain in the pure shear model (anticlockwise positive). The red line tracks rotation of the large*
461 *grain, and the blue line shows the mean rotation behaviour of matrix grains. b) Mean and*
462 *standard deviation of all grain rotations in the pure shear model. c) Angular velocity of all*
463 *grains (grey lines) as a function of strain in the pure shear model. The red line tracks the*
464 *angular velocity of the large grain, and the blue line shows the mean angular velocity of matrix*
465 *grains. For an animation of angular velocities throughout the entire evolution of the model,*
466 *see the Pure_ang_vel simulation in the supplementary materials. d) Evolution of differential*
467 *stress (i.e. strength evolution of the deforming microstructure) during the model run.*

468

469 DiffForm also models stress evolution on individual grain boundaries. Figure 5 shows grain
470 boundary stresses at four time increments throughout the experiment (readers are referred to

the Pure_stresses simulation in the supplementary materials for a 3D animation of grain boundary stress evolution during the experiment). Figure 5a shows that stresses are close to zero on most boundaries at the start of the experiment. Some higher compressional (positive) and extensional (negative) stresses are observed on boundaries with or adjacent to the large grain. In the first quarter of the experiment, stresses increase fairly homogeneously on all boundaries. When a strain of approximately 0.2 is reached, boundary stresses on a column of matrix grains above and below the large grain, in a direction parallel to the axis of maximum shortening in the model, and phase boundaries in the same column, become substantially larger than on other boundaries. The growth of these boundary stresses is most easily visualised in the Pure_stresses simulation in the supplementary materials. As strain proceeds, stress is transmitted to matrix grain boundaries in the same row of grains further from the large grain until a strain of around 0.35, when the maximum stress differences between those grain boundaries and surrounding matrix grain boundaries are reached (Fig. 5b). This coincides with the change in rotation direction of the large grain. After 0.35 strain, stresses are rapidly redistributed onto all matrix grain boundaries, and by a strain of around 0.5, stress magnitudes are roughly equal on all boundaries (Fig. 5c). Subsequently, at the same time as a large spread in angular velocities is observed to occur at a strain of around 0.6, stresses on boundaries in the initial row of grains parallel to the direction of maximum shortening drop rapidly (Fig. 5d), and this behaviour spreads throughout the matrix just before the model terminates (Fig. 5d).

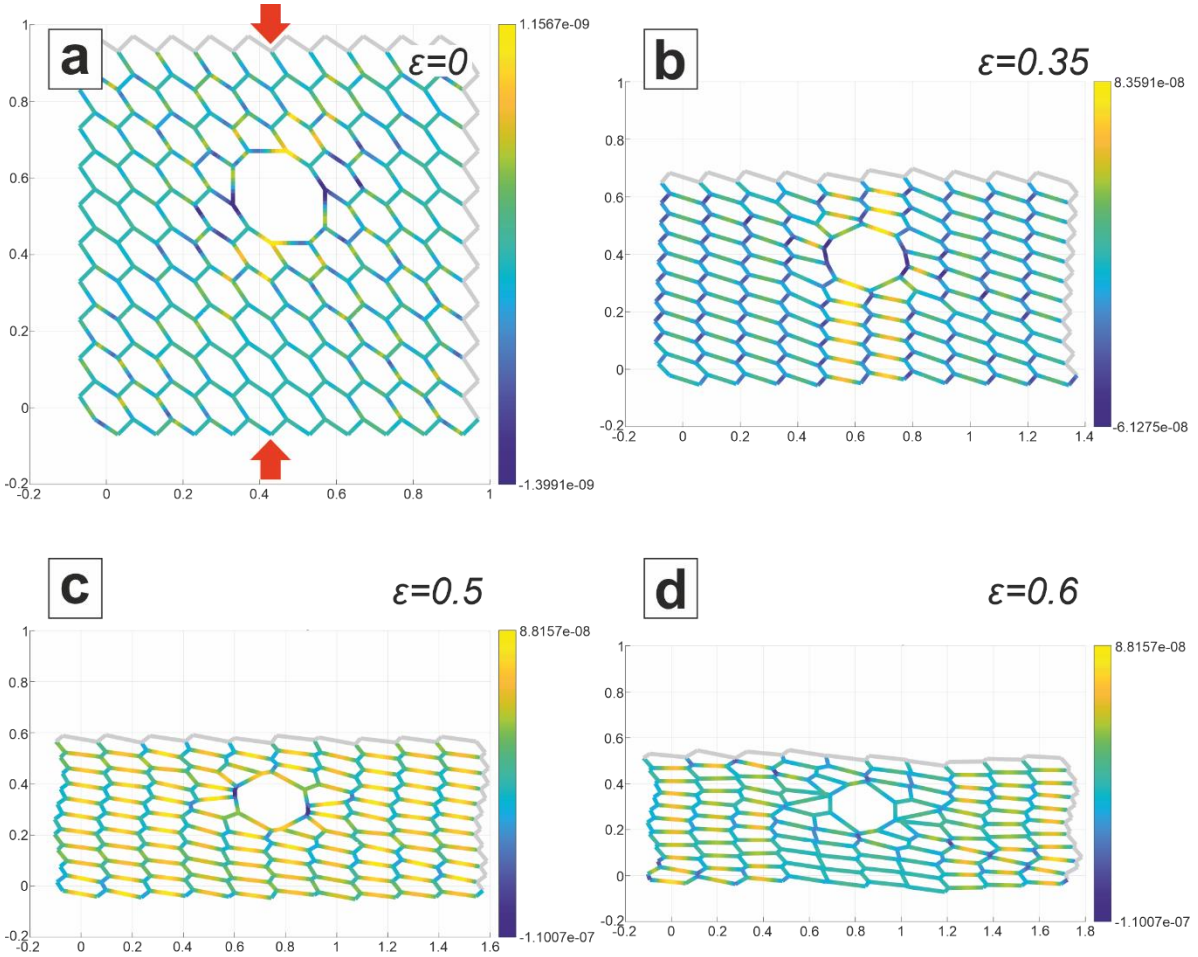

Figure 5 *Grain boundary stresses at four time increments in the pure shear model run. a) At the start of the experiment, stresses on most matrix boundaries are close to zero. Boundaries associated with the large grain show the highest positive (compressive) and negative (tensional) stresses. Red arrows show direction of shortening. b) High compressive stresses first develop on matrix grain boundaries in a column parallel to the axis of maximum shortening above and below the large grain, and on the phase boundaries between the large grain and small grains. c) As strain proceeds, compressive stress develops on other matrix boundaries. d) As the rotation direction of the large grain changes, stress on small grain-large grain phase boundaries, and matrix grain boundaries in a column parallel to the axis of maximum shortening above and below the large grain, drops substantially. With further strain, stress magnitudes on the other matrix grains also drop (see the Pure_stresses simulation in the supplementary material for a 3D animation of the full model run).*

4.2 Simple shear

Dextral simple shear was applied to the same starting geometry as the pure shear experiment (Figure 2). The dextral simple shear experiment reached a strain of 108% (215 timesteps) before terminating. Figure 6 shows four strain increments of the microstructural evolution of the model during simple shear. The Simple_fin_theta and Simple_ang_vel simulations in the supplementary materials show animations of the entire model run. The colour scheme in Figure 6 shows finite rotation of grains, in degrees. Note that the colour scale changes between plots to accommodate higher-angle finite rotations at increased strains. The simulations in the supplementary information are set up so that the colour scale limits are the same for all frames. The influence of the large grain on matrix grain rotations is quite different to that observed in pure shear, but equally noteworthy.

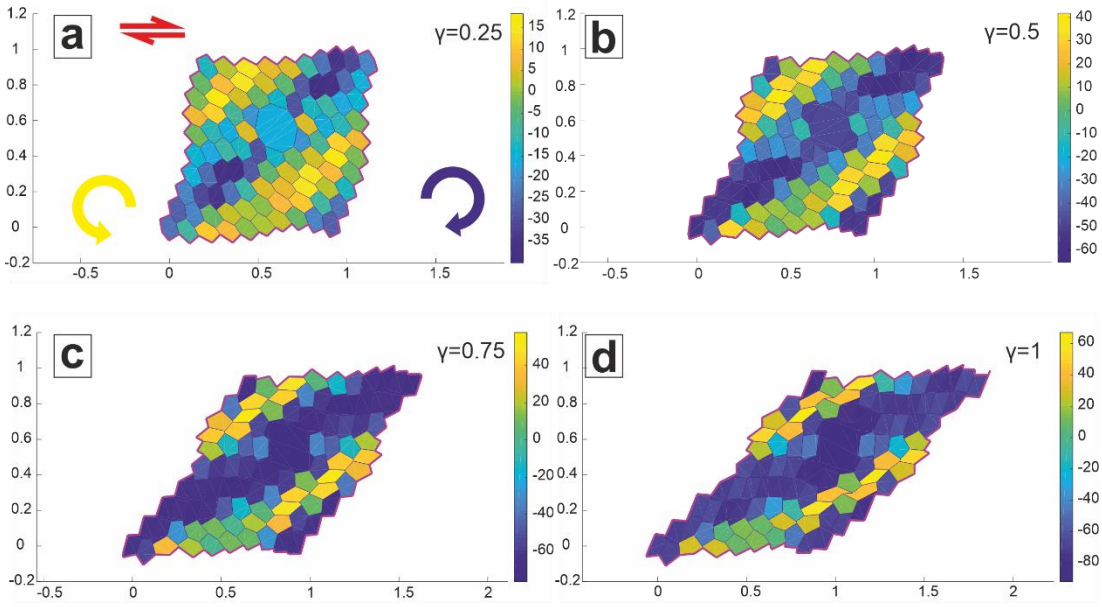

Figure 6 *Results of the simple shear experiment at four strain increments. The model terminated at a strain of 1.08. Grains are coloured by finite rotation with respect to starting orientation, in degrees (anticlockwise positive, yellow arrow in (a); clockwise negative, blue arrow in (a)). Red arrows in (a) show direction of shear. Note change in scale for each strain increment; colour scale was altered so unique features can be seen at each stage. For an*

520 *animation of finite rotations throughout the entire evolution of the model, see the*
521 *Simple_fin_theta simulation in the supplementary materials.*

522

523 Initially, the large grain begins to rotate in a clockwise direction, i.e. synthetically to the
524 imposed shear strain direction. The rotation of the large grain influences a row of grains
525 perpendicular to the shape fabric to rotate in the same direction as itself (seen as a blue band in
526 Fig. 6a–d). Rotation of these grains results in neighbouring grains forming two rows of grains
527 either side of the first (i.e. perpendicular to original shape fabric) that rotate in the opposite
528 direction (anticlockwise). The initial shape preferred orientation in the matrix is substantially
529 reduced with increasing strain. Figure 7 shows the evolution of grain shapes as best-fit ellipses,
530 using the ellipse shape averaging method reported in Wheeler (1984). The average aspect ratio
531 of the grains decreases from > 1.8 at the start of the experiment to a minimum of 1.12 at 110
532 time steps, before increasing again to 1.53 by the end of the run (Fig. 7a, which shows aspect
533 ratio evolution throughout the full model run; 215 time steps). The average orientation of the
534 long axis of grains rotates synthetically with increasing shear strain (Fig. 7b–d), i.e. clockwise,
535 but the change in average aspect ratio shows this is not simply due to rigid body rotation; grains
536 shorten in directions parallel to the shortening axis of the incremental strain ellipse, and
537 lengthen in directions parallel to the stretching axis of the incremental strain ellipse.

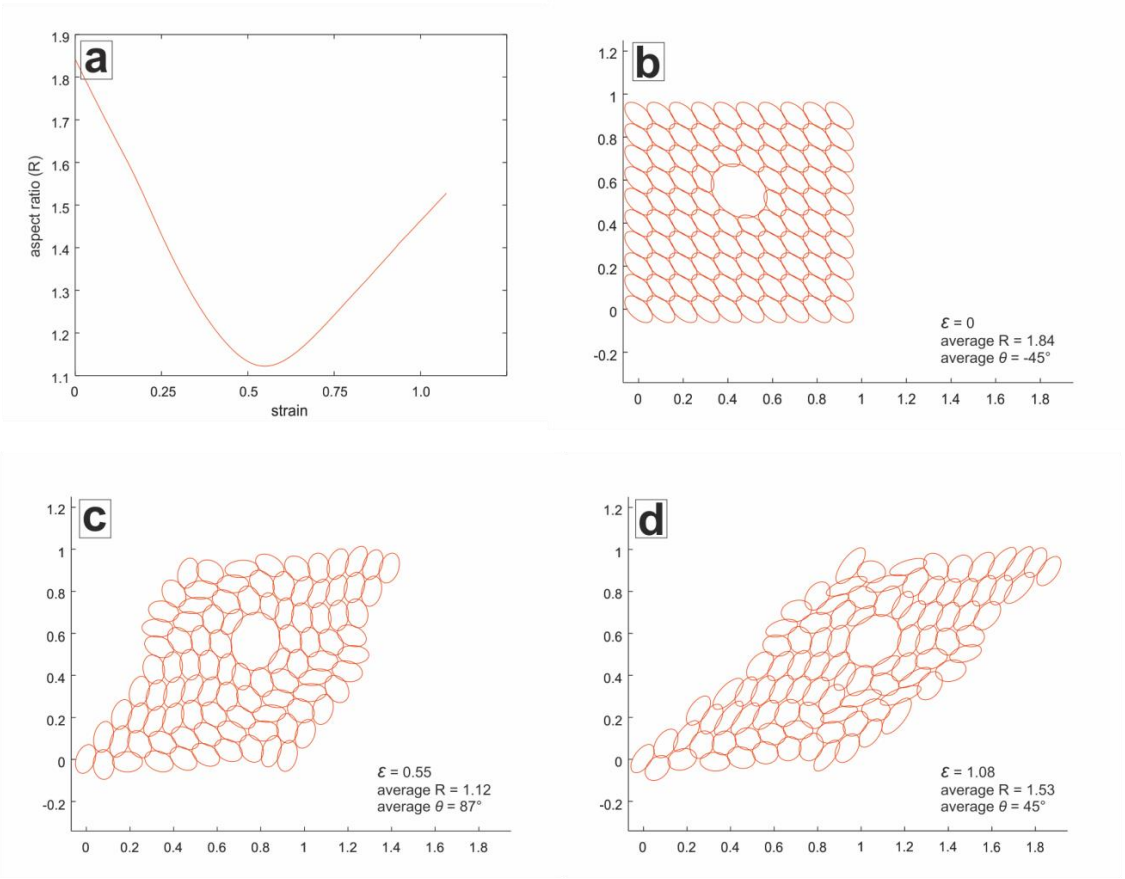

Figure 7 *a) Aspect ratio evolution during dextral simple shear. b) Best fit ellipses to grains in the starting net have an average aspect ratio (R) of 1.84, and the average angle of grain long axes to the horizontal is 45° clockwise. c) At a strain of 0.55 (half way through the model run) average aspect ratio of the best fit ellipses drops to 1.12, and on average long axes have rotated to almost vertical (87°). d) When the model run terminates, best fit ellipses have an average aspect ratio of 1.53, and long axes have continued to rotate to an average of 45° to the horizontal.*

Most grains retain their initial rotation direction for the duration of the experiment. Finite rotation over total strain is plotted for each grain in Figure 8a. Finite rotations are quite small until a strain of around 0.15, when grain rotations spread out rapidly in both rotation directions (Fig. 8a). Individual grain rotations subsequently decelerate with increasing strain, and the

mean of matrix grain rotations also flattens off, suggesting grain rotations are fairly stable (Fig. 8a–b). The standard deviation shows the spread in rotations continues to increase with strain (Fig. 8b). In Figure 8c, the angular velocity of each grain is plotted against total strain. The angular velocity plot shows a rapid increase in rotational velocity of individual grains in both rotation directions between a strain of around 0.15 to a strain of around 0.2, after which rotation velocities begin to fall. However, the mean angular velocity of the matrix grains (blue line in Fig. 8c) remains fairly constant, indicating that the increase in angular velocities in each direction is roughly the same, and suggesting that the angular velocities of matrix grains directly impact their neighbours. The angular velocities of most grains flatten off at a strain of around 0.4 and gradually evolve towards zero, again indicating evolution of the microstructure towards a rotational steady state (Wheeler, 2009). Matrix grain rotations are clearly influenced by the large grain, as they broadly follow the same pathway in both the finite rotation and angular velocity plots (Figs. 8a and c). The differential stress evolution plot shows a constant value until a strain of about 0.15 when it drops suddenly indicating a decrease in strength in the net. This drop in strength correlates with the sharp increase in the angular velocity of the large grain (and therefore all grains). As grain rotations stabilise, the differential stress curve flattens, indicating the strength of the net has stabilised at a new, but lower, value.

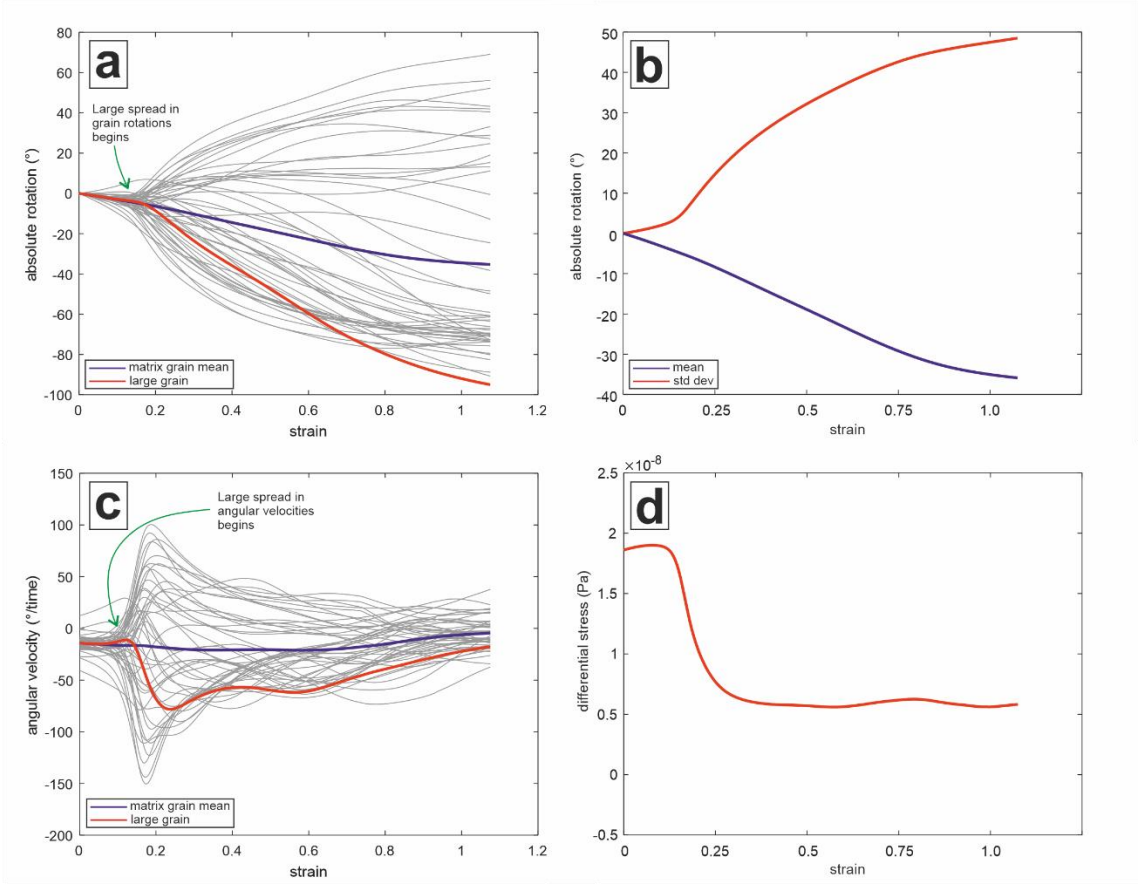

568

569 ***Figure 8*** *a) Absolute rotation, in degrees, of each grain as a function of increasing strain in*
570 *the dextral simple shear model (anticlockwise positive). The red line tracks rotation of the large*
571 *grain, and the blue line shows the mean rotation behaviour of matrix grains. b) Mean and*
572 *standard deviation of all grain rotations in the simple shear model. c) Angular velocity of all*
573 *grains as a function of strain in the simple shear model. The red line tracks the angular velocity*
574 *of the large grain, and the blue line shows the mean angular velocity of matrix grains. For an*
575 *animation of angular velocities throughout the entire evolution of the model, see the*
576 *Simple_ang_vel simulation in the supplementary materials. d) Evolution of differential stress*
577 *(i.e. strength evolution of the deforming microstructure) during the model run.*

578

579 Figure 9 provides further insight into stress evolution in the simple shear model on the grain
580 scale. In contrast to the pure shear experiment, starting stresses are not close to zero (compare

581 Fig. 9a with Fig. 5a). Similar to the pure shear experiment, however, there is a row of matrix
582 grains parallel to the maximum shortening axis and in line with the large grain that
583 experience notably higher boundary stresses than their neighbours (Fig. 9a). In the animation
584 of this model run (Simple_stresses in the supplementary materials), this band of high stress
585 boundaries can be observed to rotate, as the axis of maximum shortening also rotates with
586 increasing strain. By a strain of approximately 0.25, the band of high stress boundaries
587 becomes obscured by stress on most other boundaries building to similar magnitudes (Fig.
588 9b). As strain proceeds, stress magnitudes on nearly all matrix boundaries drop substantially,
589 which appears to re-focus stress on boundaries associated with the large grain, so that at a
590 strain of around 0.5, a band of high stress boundaries reappears, in line with the large grain
591 and parallel to the axis of maximum shortening (Fig. 9c). Stress on other matrix grains then
592 builds again to obscure this band after a strain of around 0.9 (Fig. 9d), before the model
593 terminates.

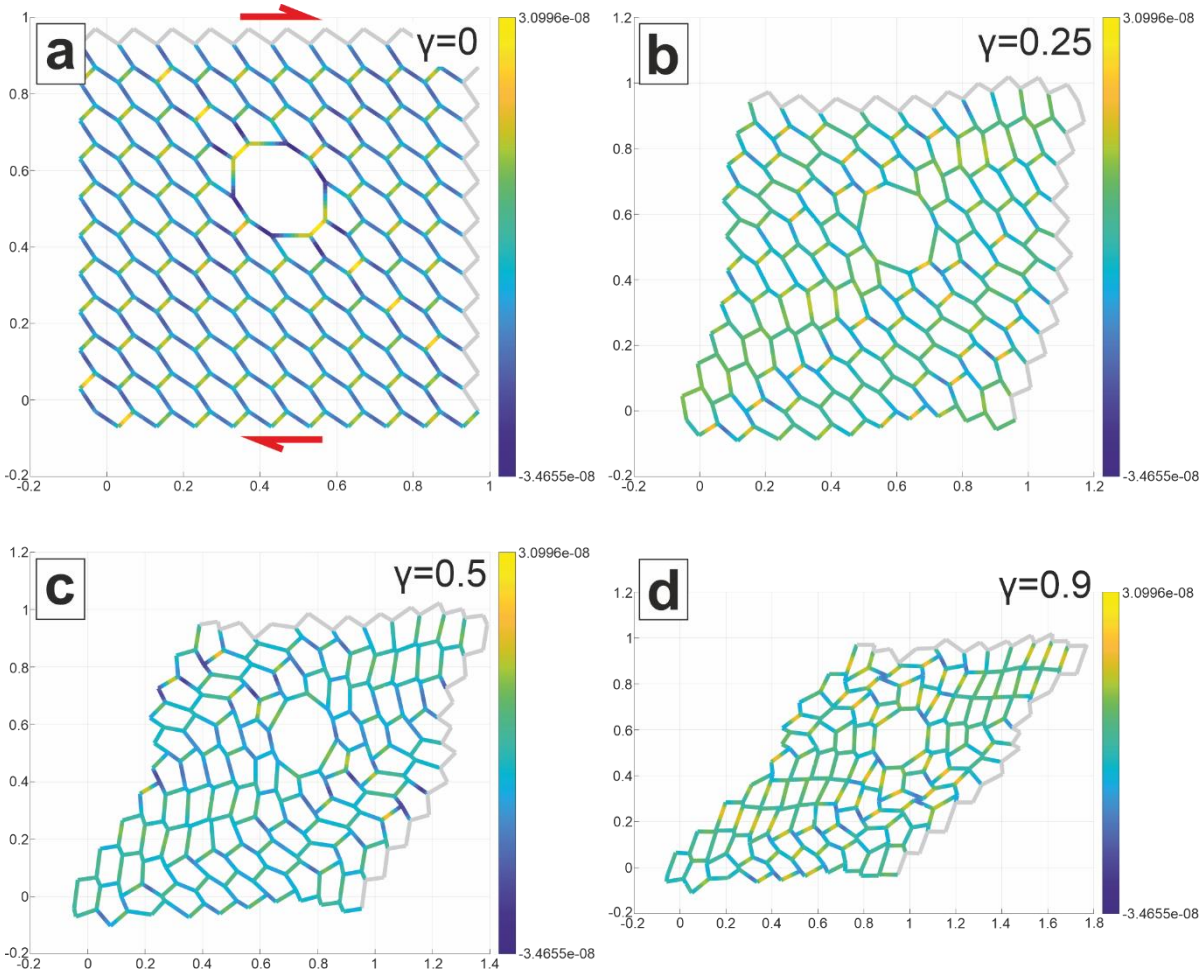

Figure 9 *Grain boundary stresses at four time increments in the simple shear model run. a) At the start of the simple shear run, grain boundaries experience noticeable stress. A row of grains with larger boundary stresses runs top left to bottom right through the net due to the presence of the large grain, similar to pure shear (compare Fig. 5b and see 3D simulation Simple_stresses in the supplementary materials). b) As strain proceeds, stresses on all grain boundaries evolve to similar magnitudes, similar to pure shear. c) After a drop in stress on all boundaries, as also seen in pure shear, boundary stresses begin to build again on a row of grains associated with the large grain (see also the 3D simulation Simple_stresses in the supplementary materials). d) As strain proceeds, stresses on all boundaries evolve to similar magnitudes again, suggesting the pattern in both pure and simple shear may be cyclical (see the Simple_stresses simulation in the supplementary material for an animation of the full model run).*

5 Discussion

5.1 Grain rotations

The rotation of large grains within a fine-grained matrix has received a considerable amount of attention from the microstructural modelling community in the last few decades (e.g., Fay et al., 2008; Griera et al., 2011; Griera et al., 2013; Johnson, 2009), primarily because porphyroblast/clast rotation microstructures are routinely used in the interpretation of strain histories. To date, models have tended to focus on deformation in the dislocation creep regime. Because grain rotations are inherent to diffusion creep, which is promoted at finer grain sizes, it is also important to assess the effects that diffusion creep in a fine-grained matrix may have on the rotation of large grains. Grain rotations during diffusion creep occur in a very dynamic environment, where rotations have a measurable impact on adjacent grains. In particular, rotations of large grains can have significant effects on the surrounding matrix. Rotations of large grains are generally assumed to be either synthetic or antithetic to shear (Griera et al., 2013). The results presented here suggest a more complex picture, where the rotation direction of the large grain can in fact change over time as the large and matrix grains interact (Fig. 4a), which in turn can lead to significant changes in local stress distributions (Fig. 5) and an associated drop in strength (Fig. 4d). This observation has significant implications for the extrapolation of strain histories from microstructures. For example, metamorphic garnets are commonly littered with inclusions whose distributions are interpreted as regional-scale shear sense indicators. If local changes in the rotation direction of large grains can occur due to interactions between large and matrix grains during pressure solution/diffusion creep, relatively simple imposed strain paths could potentially give rise to microstructures that might be interpreted as the product of vastly more complicated strain histories, e.g. a single deformation phase may erroneously be interpreted as multiphase (Fossen et al., 2019). The counter argument to this is that inclusion trails are often observed to be correlated between

632 different porphyroblasts on the outcrop to regional scale (Aerden, 1995; Aerden and Ruiz-
633 Fuentes, 2020; Fay et al., 2008; Johnson, 1990; Steinhardt, 1989), and if inclusion trail patterns
634 resulted from locally turbulent behaviour, it would be impossible for them to maintain
635 regionally consistent orientations. Further, it would be impossible for different age sets of
636 porphyroclasts to develop distinct inclusion trail sets with regionally-consistent orientations
637 (Aerden et al., 2020; Aerden and Ruiz-Fuentes, 2020). However, it is not always the case that
638 inclusion trails in a single sample have consistent orientations. For example, Johnson et al.,
639 (2006) analysed staurolite inclusion trails in low-pressure, high-temperature schists that formed
640 during the development of crenulation cleavage, finding a spread in inclusion trail orientations
641 of 40–75° that provided clear evidence for the large staurolite grains rotating relative to one
642 another and to the crenulation cleavage. More detailed modelling on the evolution of grain
643 rotations to very high strains, and their effects on stress distributions on the grain scale, would
644 give valuable insight into how finite strain microstructures should be interpreted. Of particular
645 use would be DiffForm models that included more than one large grain, so their relative
646 rotations could be analysed. At present, there are computational constraints on constructing
647 and running such starting geometries in DiffForm (see section 5.4.2).

648 In the current model runs, rotations of matrix grains are clearly influenced by the presence of
649 the large grain. In the pure shear model, the presence of the large grain appears to affect the
650 overall strength the microstructure by suppressing the rotations of certain grains, which results
651 in stress build-up on specific boundaries. The local distribution of stress in this case happens
652 to lead to an alignment of grain boundaries, which acts as a plane of weakness within the net.
653 The inference here is that a rock comprised of grains with a homogeneous grain size deforming
654 by diffusion creep may be stronger than those with greater diversity of grain size, because large
655 grains can act to focus stresses, and resultant microstructural modifications inherent in
656 diffusion creep, into specific areas. This can result in the development of mechanical

heterogeneities that weaken the bulk rock, and may lead to weak zones/decoupling of interfaces around large grains similar to those previously modelled in the dislocation creep regime (Griera et al., 2011).

5.2 Preservation or formation of a CPO

Shape preferred orientations (SPOs) have been observed to develop during diffusion creep (e.g. Díaz Aspiroz et al., 2007; Getsinger and Hirth, 2014; Imon et al., 2004), and CPOs can develop in tandem with an SPO. Furthermore, it has been shown that inherited CPOs can be retained during diffusion creep deformation (Jiang et al., 2000; Wheeler, 2009). In the pure shear experiment performed here, a CPO would not be expected to develop from a random initial texture, as the rotations of all grains follow the same path, i.e. all grains largely rotate the same amount, and in the same direction, so the initial random texture is preserved. However, if there was an initial CPO in the matrix grains of such a rock, it would be largely preserved, albeit weakened, by the diffusion creep deformation. A starting net with a more heterogeneous grain size may evolve quite differently so further work is required in this area.

In the simple shear experiment, the story is more complex but follows the same trend; a rock with no initial crystallographic alignment would not develop one during diffusion creep deformation. However, if an initial CPO did exist, crystallographic alignment would also be observed in the final geometry, but the original CPO would have been split into two smaller CPO 'domains' – one whose grains share an orientation because they rotated in the same direction as the large grain, and another whose grains share a different orientation, related to rotation directions that are antithetic to the large grain rotation direction, but share the same direction and velocity as one another, so any initial shared orientation is preserved during rotation.

5.3 Strength evolution

Grain rotations have effects beyond those on the rock's texture. Microstructure influences the physical properties of deforming crystalline materials, and the experimental results presented here clearly indicate that the strength of a rock (or other crystalline material) deforming by diffusion creep can be influenced by grain rotations. When rotations are large and fast, the microstructure can be interpreted to 'destabilise' (i.e. transiently evolve away from overall steady-state behaviour; Figs. 4c and 8c), with an associated drop in strength (Figs. 4d and 8d), in both pure and simple shear. This transient behaviour appears to be controlled by how rapid the rotation of the large grain is within the fine-grained matrix. Again, it is the heterogeneity in the microstructure that causes these effects.

The presence of a large insoluble grain is also shown to affect the local distribution of grain boundary stresses, with those grains in closest proximity to and in line with the large grain parallel to the axis of maximum shortening experiencing a greater magnitude and more rapid build-up of stress than other matrix grains (Figs. 5 and 9). In pure shear, the change in rotation direction appears to have a profound effect on the way stresses are distributed on boundaries throughout the model, with high stresses rapidly redistributed away from the single row of grains to all other boundaries (Fig. 5). A similar pattern of stress redistribution behaviour occurs in the simple shear run, but the sequence of i) a build-up of stresses close to the large grain before ii) redistribution onto matrix grains, followed by iii) a drop in stress on all boundaries, appears to at least begin a second cycle. This can best be seen in the Pure_stresses and Simple_stresses animations in the supplementary information. The suggestion of such cyclical behaviour warrants further investigation to higher strains.

The low stress values shown in Figures 4d and 8d are a result of legacy values for some coefficients used during model development: in section 2 we showed that for equivalent size spheres $\eta = 1.461 \times 10^{-8}$ Pa.s. For simple shear (Figs.6–9), the shear strain rate is $\dot{\gamma} = 0.5\ s^{-1}$,

705 so the equivalent differential stress (twice the shear stress) is 1.5 x 10^{-8} Pa. This value is of a
706 similar order of magnitude to the starting value of differential stress in the model, which is 1.9
707 x 10^{-8} Pa. The theoretical value is slightly lower than the modelled value because elongate
708 grains are stronger than equant grains of equivalent area; e.g. Elliott (1973) showed that at
709 constant stress, grain elongation results in a decrease in strain rate. Moreover, Coble's (1963)
710 derivation is for notional spherical grains. These provide diffusion pathways in all three
711 dimensions and so strength is lower than for "two-dimensional" grains which in effect have
712 infinite length in the third dimension.

713 The initial strength of the net in pure shear was close to zero (Figs. 4d & 5a). Wheeler (2010)
714 discussed anisotropic rheology during diffusion creep, with particular reference to a periodic
715 microstructure constructed of a single irregular hexagonal grain shape. The results of Wheeler
716 (2010) showed that anisotropy occurred in two orthogonal strong directions, and two
717 orthogonal weak directions that lie at 45° to the strong directions. The model runs in this study
718 were set up so that grain boundaries had zero viscosity, and, under these conditions, the weak
719 directions have low strength. The large grain was expected to have some effect on the strength
720 of the starting net, but it seems to have been minor. The initial very low strength of this net is
721 explained by the fact that the elongate hexagons which comprised the initial microstructure
722 were oriented in such a way that the direction of imposed pure shear happened to be aligned
723 with the weak directions. As finite grain rotations occurred, the strength of the microstructure
724 increased as the weak directions rotated away from parallelism with the imposed shear stress
725 (Fig. 4d).

726 A periodic microstructure can create spurious results in models of diffusion creep, as discussed
727 below in section 5.4. In pure shear, alignment of matrix grain boundaries is considered to lead
728 to the observed drop in strength. Could the periodicity in the starting net be the reason for
729 boundary alignment and associated strength drop? This is not thought to be the case, as sliding

surfaces nearly always develop due to boundary alignment in starting nets with heterogeneous grain geometry during diffusion creep, and affect the strength of the nets in the same way as observed here (Wheeler, 2009, and unpublished models). Thus, boundary alignment is simply a natural product of diffusion creep deformation. The results of both the pure and simple shear simulations show that the presence of large grains will influence where within the microstructure such boundary alignment (and therefore sample weakening) will occur.

5.4 Model limitations and future work

5.4.1 Effect of a periodic matrix on microstructure evolution

Although many natural rocks do exhibit an SPO, the geometry of the matrix grains in the start net used here is somewhat artificial. Such periodicity of grain shape can cause problems in diffusion creep modelling because the neighbour switches that occur as a natural product of diffusion-accommodated grain boundary sliding (Spingarn and Nix, 1978) all occur at the same time throughout the microstructure. Such synchronised grain switching is unrealistic and thus will produce a somewhat simplified deformation behaviour. In addition, the grain shape anisotropy in our starting net is orientated at 45° to the maximum shortening axis of the instantaneous strain ellipse in both the pure shear and simple shear model runs. As discussed in section 5.3, Wheeler (2010) showed that irregular hexagons develop an anisotropic rheology in diffusion creep, so that a polycrystal made of repeating hexagons exhibits an overall anisotropic rheology in DiffForm models (see Fig. 4 of Wheeler, 2010. The effect of this anisotropy is reflected in the stress evolution of the pure shear and simple shear models presented here (Figs. 4d and 8d). Work in progress suggests there is a rigorous mathematical basis to expect anisotropic rheology will also develop in more irregular microstructures, with initial results comparable to those presented in Figure 4 of Wheeler (2010). Therefore, we do not expect the initial shape anisotropy of our starting nets to have spuriously influenced evolution of the microstructure.

The advantage of a mostly-periodic matrix is that it is easy to identify differences in the behaviour of matrix grains that are a result of (in this case) the presence of a large grain. Despite the differences between the simplified starting net and natural microstructures, such modelling is an important first step in understanding how microstructural evolution proceeds in crystalline materials with grain size heterogeneity during diffusion creep. Further work on more realistic, heterogeneous starting geometries is necessary to elucidate the effects of large grains on stress, grain rotations, and other aspects of microstructural evolution in real rocks.

5.4.2 Relative size of large grain and matrix grains

In the current model microstructure, the second phase grain is an order of magnitude larger than the matrix grains. Porphyroblasts in natural rocks have cross-sectional areas that are commonly 3 to 4 orders of magnitude larger than matrix grains (e.g. Vernon, 2018), meaning many more matrix grains lie adjacent to large grains. At present, this difference in grain size cannot be modelled in DiffForm due to issues with boundary switching at key nodes that compose grain boundaries lining the edge of the model net. When a finer matrix grain size is used, greater issues with boundary switching lead to model runs terminating at low strain, before much microstructural change has occurred. Similarly, it would be insightful to compare the behaviour of more than one large grain within a single experiment, but this cannot currently be achieved due to constraints on the smallest workable matrix grain size. Solving this issue is an important next step in the future development of the DiffForm modelling suite.

We speculate that an increased difference in relative size of large and matrix grains is unlikely to substantially change the rotational behaviour of large grains from that observed here. A finer grain size would make the matrix weaker (due to grain boundary diffusion creep having a grain size exponent of 3 in Eq. 2; Poirier, 1985), which may decrease the rotational stability of the large grain. However, the ductility contrast between the two phases is already defined to be (almost) infinite in the model, so the relative weakness of the matrix with respect to the large

grain would not noticeably change. One instance where a greater number of fine grains lining a porphyroblast boundary could potentially arrest rotation behaviour is if those fine grains all rotated in the opposite direction to their neighbours, as observed in the simple shear model, in such a way that the resulting sum of traction on all large grain boundary segments was equal to zero. However, in a matrix where grain shapes show greater heterogeneity, as observed in nature, it is difficult to see this scenario occurring.

6 Conclusions

During the microstructural evolution of a fine-grained matrix undergoing diffusion creep:

1) Rotations of matrix grains are strongly influenced by rotation of large grains, especially matrix grains that lie adjacent to large grains.
2) The rotation direction of a large grain does not have to be simply either synthetic or antithetic; rotation directions can change due to interactions with the matrix, and the overall evolution of grain rotations in a rock undergoing diffusion creep is complex.
3) The presence of large grains is unlikely to influence formation of a CPO. However, a pre-existing CPO can be largely preserved, and depending on the shear geometry may be split into smaller domains due to the influence that large grain rotation has on matrix grains.
4) Large grains create stress heterogeneities that focus the effects of diffusion creep. This can influence how and where grain boundaries align within a microstructure, which can lead to a profound drop in strength of a material.
5) The local distribution of matrix grain boundary stresses is clearly influenced by proximity to large second phase grains. Stresses are greater on boundaries oriented favourably to the axis of maximum shortening. The model results suggest some kind of cyclical transfer of stress into different parts of the matrix may occur during diffusion creep, which is influenced by switches in the rotation direction of large grains.

6) An increase in the velocity of a rotating large grain can lead to the angular velocities of matrix grain rotations transiently evolving away from steady-state, which results in a significant drop in the strength of a material deforming by diffusion creep. However, individual grain rotations can return to a steady-state, which re-stabilises the strength of the material, but at a value lower than the starting strength.

Acknowledgements

This work was supported by the Natural Environment Research Council [grant number NE/L002469/1]. We thank L. Evans (Monash University), R. Gardner (Macquarie University) and S. Piazolo (University of Leeds) for the translated form of the input net. D. Aerden and one anonymous reviewer are thanked for their insightful reviews. V. Toy is thanked for editorial handling of the manuscript.

817 **References**

818 Aerden, D., Sayab, M., Forde, A., Ruiz-Fuentes, A., 2020. Kinematics of subduction in the
819 Ibero-Armorican arc constrained by 3D microstructural analysis of garnet and
820 pseudomorphed lawsonite porphyroblasts from Ile de Groix (Variscan belt). Solid Earth
821 Discuss. 2020, 1-36.
822 Aerden, D.G.A.M., 1995. Porphyroblast non-rotation during crustal extension in the Variscan
823 Lys-Caillaouas Massif, Pyrenees. Journal of Structural Geology 17, 709-725.
824 Aerden, D.G.A.M., Ruiz-Fuentes, A., 2020. X-ray computed micro-tomography of spiral
825 garnets: A new test of how they form. Journal of Structural Geology 136, 104054.
826 Ammann, M.W., Brodholt, J.P., Wookey, J., Dobson, D.P., 2010. First-principles constraints
827 on diffusion in lower-mantle minerals and a weak D″ layer. Nature 465, 462-465.
828 Ashby, M.F., Verrall, R.A., 1973. Diffusion-accommodated flow and superplasticity. Acta
829 Metallurgica 21, 149-163.
830 Bell, T. H., Cuff, C., 1989. Dissolution, solution transfer, diffusion versus fluid flow and
831 volume loss during deformation/metamorphism. Journal of Metamorphic Geology 7(4), 425-
832 447.
833 Bell, T.H., Ham, A.P., Kim, H.S., 2004. Partitioning of deformation along an orogen and its
834 effects on porphyroblast growth during orogenesis. Journal of Structural Geology 26, 825-
835 845.
836 Bell, T.H., Johnson, S.E., 1989. Porphyroblast inclusion trails: the key to orogenesis. Journal
837 of Metamorphic Geology 7, 279-310.
838 Berton, J.R., Durney, D.W., Wheeler, J., 2011. Diffusion-creep modelling of fibrous pressure
839 shadows II: influence of inclusion size and interface roughness. Geological Society, London,
840 Special Publications 360, 319.

841 Berton, J.R., Durney, D.W., Wheeler, J., Ford, J.M., 2006. Diffusion-creep modelling of
842 fibrous pressure-shadows. Tectonophysics 425, 191-205.
843 Bons, P.D., den Brok, B., 2000. Crystallographic preferred orientation development by
844 dissolution–precipitation creep. Journal of Structural Geology 22, 1713-1722.
845 Bons, P., Koehn, D., & Jessell, M. W. (Eds.). (2007). Microdynamics simulation.
846 Lecture Notes in Earth Sciences (Vol. 106). Springer, Berlin.
847 Bucher, K., Stober, I., 2010. Fluids in the upper continental crust. Geofluids 10, 241-253.
848 Carreras, J., Cosgrove, J.W., Druguet, E., 2013. Strain partitioning in banded and/or
849 anisotropic rocks: Implications for inferring tectonic regimes. Journal of Structural Geology
850 50, 7-21.
851 Coble, R.L., 1963. A Model for Boundary Diffusion Controlled Creep in Polycrystalline
852 Materials. Journal of Applied Physics 34, 1679-1682.
853 Dabrowski, M., Schmid, D.W., Podladchikov, Y.Y., 2012. A two-phase composite in simple
854 shear: Effective mechanical anisotropy development and localization potential. Journal of
855 Geophysical Research: Solid Earth 117.
856 Díaz Aspiroz, M., Lloyd, G.E., Fernández, C., 2007. Development of lattice preferred
857 orientation in clinoamphiboles deformed under low-pressure metamorphic conditions. A
858 SEM/EBSD study of metabasites from the Aracena metamorphic belt (SW Spain). Journal of
859 Structural Geology 29, 629-645.
860 Elliott, D., 1973. Diffusion Flow Laws in Metamorphic Rocks. GSA Bulletin 84, 2645-2664.
861 Fay, C., Bell, T.H., Hobbs, B.E., 2008. Porphyroblast rotation versus nonrotation: Conflict
862 resolution! Geology 36, 307-310.
863 Ford, J.M., Ford, N.J., Wheeler, J., 2004. Simulation of grain-boundary diffusion creep:
864 analysis of some new numerical techniques. Proceedings of the Royal Society of London.
865 Series A: Mathematical, Physical and Engineering Sciences 460, 2395.

866 Ford, J.M., Wheeler, J., Movchan, A.B., 2002. Computer simulation of grain-boundary
867 diffusion creep. Acta Materialia 50, 3941-3955.
868 Fossen, H., Cavalcante, G.C.G., Pinheiro, R.V.L., Archanjo, C.J., 2019. Deformation –
869 Progressive or multiphase? Journal of Structural Geology 125, 82-99.
870 Getsinger, A.J., Hirth, G., 2014. Amphibole fabric formation during diffusion creep and the
871 rheology of shear zones. Geology 42, 535-538.
872 Gómez Barreiro, J., Lonardelli, I., Wenk, H.R., Dresen, G., Rybacki, E., Ren, Y., Tomé,
873 C.N., 2007. Preferred orientation of anorthite deformed experimentally in Newtonian creep.
874 Earth and Planetary Science Letters 264, 188-207.
875 Gratier, J.-P., Dysthe, D.K., Renard, F., 2013. The role of pressure solution creep in the
876 ductility of the Earth's upper crust. Advances in Geophysics 54, 47-179.
877 Griera, A., Bons, P.D., Jessell, M.W., Lebensohn, R.A., Evans, L., Gomez-Rivas, E., 2011.
878 Strain localization and porphyroclast rotation. Geology 39, 275-278.
879 Griera, A., Llorens, M.-G., Gomez-Rivas, E., Bons, P.D., Jessell, M.W., Evans, L.A.,
880 Lebensohn, R., 2013. Numerical modelling of porphyroclast and porphyroblast rotation in
881 anisotropic rocks. Tectonophysics 587, 4-29.
882 Hiraga, T., Miyazaki, T., Tasaka, M., Yoshida, H., 2010. Mantle superplasticity and its self-
883 made demise. Nature 468, 1091-1094.
884 Hirth, G., Kohlstedt, D.L., 1995. Experimental constraints on the dynamics of the partially
885 molten upper mantle: Deformation in the diffusion creep regime. Journal of Geophysical
886 Research: Solid Earth 100, 1981-2001.
887 Holcombe, R.J., Little, T.A., 2001. A sensitive vorticity gauge using rotated porphyroblasts,
888 and its application to rocks adjacent to the Alpine Fault, New Zealand. Journal of Structural
889 Geology 23, 979-989.

890 Imon, R., Okudaira, T., Kanagawa, K., 2004. Development of shape- and lattice-preferred
891 orientations of amphibole grains during initial cataclastic deformation and subsequent
892 deformation by dissolution–precipitation creep in amphibolites from the Ryoke metamorphic
893 belt, SW Japan. Journal of Structural Geology 26, 793-805.
894 Jessell, M.W., Bons, P.D., Griera, A., Evans, L.A., Wilson, C.J.L., 2009. A tale of two
895 viscosities. Journal of Structural Geology 31, 719-736.
896 Jiang, Z., Prior, D.J., Wheeler, J., 2000. Albite crystallographic preferred orientation and
897 grain misorientation distribution in a low-grade mylonite: implications for granular flow.
898 Journal of Structural Geology 22, 1663-1674.
899 Johnson, S.E., 1990. Lack of porphyroblast rotation in the Otago schists, New Zealand:
900 implications for crenulation cleavage development, folding and deformation partitioning.
901 Journal of Metamorphic Geology 8, 13-30.
902 Johnson, S.E., 1993. Unravelling the spirals: a serial thin-section study and three-dimensional
903 computer-aided reconstruction of spiral-shaped inclusion trails in garnet porphyroblasts.
904 Journal of Metamorphic Geology 11, 621-634.
905 Johnson, S.E., 2008. The effects of strain localisation on rigid-object kinematics, In: Bons,
906 P.D., Koehn, D., Jessell, M.W. (Eds.), Microdynamics Simulation. Lecture Notes in Earth
907 Sciences. Springer, Berlin, pp. 246-252.
908 Johnson, S.E., 2009. Porphyroblast rotation and strain localization: Debate settled! Geology
909 37, 663-666.
910 Karato, S.-i., Jung, H., Katayama, I., Skemer, P., 2008. Geodynamic Significance of Seismic
911 Anisotropy of the Upper Mantle: New Insights from Laboratory Studies. Annual Review of
912 Earth and Planetary Sciences 36, 59-95.
913 Karato, S.-I., Li, P., 1992. Diffusion Creep in Perovskite: Implications for the Rheology of
914 the Lower Mantle. Science 255, 1238.

915 Karato, S.-i., Wu, P., 1993. Rheology of the Upper Mantle: A Synthesis. Science 260, 771-
916 778.
917 Karato, S.-i., Zhang, S., Wenk, H.-R., 1995. Superplasticity in Earth's Lower Mantle:
918 Evidence from Seismic Anisotropy and Rock Physics. Science 270, 458.
919 Kilian, R., Heilbronner, R., Stünitz, H., 2011. Quartz grain size reduction in a granitoid rock
920 and the transition from dislocation to diffusion creep. Journal of Structural Geology 33, 1265-
921 1284.
922 Menegon, L., Pennacchioni, G., Spiess, R., 2008. Dissolution-precipitation creep of K-
923 feldspar in mid-crustal granite mylonites. Journal of Structural Geology 30, 565-579.
924 Miyazaki, T., Sueyoshi, K., Hiraga, T., 2013. Olivine crystals align during diffusion creep of
925 Earth's upper mantle. Nature 502, 321-326.
926 Mohiuddin, A., Karato, S.-i., Girard, J., 2020. Slab weakening during the olivine to
927 ringwoodite transition in the mantle. Nature Geoscience 13, 170-174.
928 Passchier, C.W., Trouw, R.A., 2005. Microtectonics. Springer Science & Business Media.
929 Piazolo, S., Jessell, M.W., Bons, P.D., Evans, L., Becker, J.K., 2010. Numerical simulations
930 of microstructures using the Elle platform: A modern research and teaching tool. Journal of
931 the Geological Society of India 75, 110-127.
932 Poirier, J., 1985. Creep of crystals. Cambridge University Press, Cambridge.
933 Raj, R., Ashby, M.F., 1971. On grain boundary sliding and diffusional creep. Metallurgical
934 Transactions 2, 1113-1127.
935 Ritterbex, S., Carrez, P., Cordier, P., 2020. Deformation across the mantle transition zone: A
936 theoretical mineral physics view. Earth and Planetary Science Letters 547, 116438.
937 Rosenberg, C.L., Stünitz, H., 2003. Deformation and recrystallization of plagioclase along a
938 temperature gradient: an example from the Bergell tonalite. Journal of Structural Geology 25,
939 389-408.

940 Rosenfeld, J. L. (1970). Rotated garnets in metamorphic rocks (Vol. 129). Geological Society
941 of America.
942 Rutter, E., 1976. The kinetics of rock deformation by pressure solution. Philosophical
943 Transactions of the Royal Society of London A: Mathematical, Physical and Engineering
944 Sciences 283, 203-219.
945 Rutter, E.H., 1983. Pressure solution in nature, theory and experiment. Journal of the
946 Geological Society 140, 725-740.
947 Rybacki, E., Dresen, G., 2000. Dislocation and diffusion creep of synthetic anorthite
948 aggregates. Journal of Geophysical Research: Solid Earth 105, 26017-26036.
949 Rybacki, E., Gottschalk, M., Wirth, R., Dresen, G., 2006. Influence of water fugacity and
950 activation volume on the flow properties of fine-grained anorthite aggregates. Journal of
951 Geophysical Research: Solid Earth 111.
952 Shelley, D., 1977. Plagioclase Preferred Orientation in Haast Schist, New Zealand. The
953 Journal of Geology 85, 635-644.
954 Skemer, P., Hansen, L.N., 2016. Inferring upper-mantle flow from seismic anisotropy: An
955 experimental perspective. Tectonophysics 668, 1-14.
956 Spingarn, J.R., Nix, W.D., 1978. Diffusional creep and diffusionally accommodated grain
957 rearrangement. Acta Metallurgica 26, 1389-1398.
958 Steinhardt, C., 1989. Lack of porphyroblast rotation in noncoaxially deformed schists from
959 Petrel Cove, South Australia, and its implications. Tectonophysics 158, 127-140.
960 Sundberg, M., Cooper, R.F., 2008. Crystallographic preferred orientation produced by
961 diffusional creep of harzburgite: Effects of chemical interactions among phases during plastic
962 flow. Journal of Geophysical Research 113.

963 Tullis, J., Yund, R., 1992. Chapter 4 The Brittle-Ductile Transition in Feldspar Aggregates:
964 An Experimental Study, in: Evans, B., Wong, T.-f. (Eds.), International Geophysics.
965 Academic Press, pp. 89-117.
966 Vernon, R.H., 2018. A practical guide to rock microstructure. Cambridge University Press,
967 Cambridge, UK.
968 Wheeler, J., 1984. A new plot to display the strain of elliptical markers. Journal of Structural
969 Geology 6, 417-423.
970 Wheeler, J., 1987. The significance of grain-scale stresses in the kinetics of metamorphism.
971 Contributions to Mineralogy and Petrology 97, 397-404.
972 Wheeler, J., 1992. Importance of pressure solution and coble creep in the deformation of
973 polymineralic rocks. Journal of Geophysical Research 97, 4579.
974 Wheeler, J., 2009. The preservation of seismic anisotropy in the Earth's mantle during
975 diffusion creep. Geophysical Journal International 178, 1723-1732.
976 Wheeler, J., 2010. Anisotropic rheology during grain boundary diffusion creep and its
977 relation to grain rotation, grain boundary sliding and superplasticity. Philosophical Magazine
978 90, 2841-2864.
979 Wheeler, J., Ford, J.M., 2008. Diffusion creep, in: Bons, P.D., Koehn, D., Jessell, M.W.
980 (Eds.), Microdynamics Simulation. Springer-Verlag, Berlin Heidelberg, p. 405.
981 Williams, P.F., Jiang, D., 1999. Rotating garnets. Journal of Metamorphic Geology 17, 367-
982 378.
983 Wintsch, R., Yi, K., 2002. Dissolution and replacement creep: a significant deformation
984 mechanism in mid-crustal rocks. Journal of Structural Geology 24, 1179-1193.
985 Zhao, N., Hirth, G., Cooper, R.F., Kruckenberg, S.C., Cukjati, J., 2019. Low viscosity of
986 mantle rocks linked to phase boundary sliding. Earth and Planetary Science Letters 517, 83-
987 94.